Article

First-Principles DFT Insights into the Stabilization of Zinc Diphosphide (ZnP$_2$) Nanocrystals via Surface Functionalization by 4-Aminothiophenol for Photovoltaic Applications

Barbara Farkaš, Aleksandar Živković, Veikko Uahengo, Nelson Y. Dzade,* and Nora H. de Leeuw

Read Online

ACCESS | Metrics & More | Article Recommendations | Supporting Information

ABSTRACT: The resurgence of interest in zinc phosphide compounds as efficient solar absorbers has initiated increasing efforts to improve their stability under humid and oxygen-rich conditions. Although organic functionalization has been suggested as a promising strategy to passivate zinc phosphide nanoparticles, fundamental atomic-level insights into the adsorption processes and structures at zinc diphosphide (ZnP$_2$) surfaces are still lacking. In this study, the interactions between 4-aminothiophenol and the low-Miller index surfaces of monoclinic ZnP$_2$ have been investigated by means of density functional theory calculations. A bidentate adsorption mode, in which 4-aminothiophenol binds through both its functional groups via Zn−N and Zn−S bonds, was predicted to be the strongest form of interaction, and monolayer-functionalized ZnP$_2$ surfaces were found to be highly stable under adsorbate-rich conditions. Changes in the equilibrium morphology of ZnP$_2$ nanocrystallites upon functionalization and effects of humidity are also discussed. The results are expected to contribute toward the rational design of ZnP$_2$-based materials for photovoltaic (PV) devices.

KEYWORDS: zinc diphosphide, 4-aminothiophenol, DFT, functionalization, photovoltaics
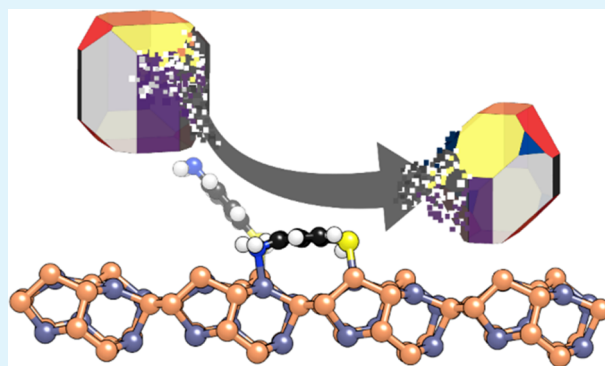
1. INTRODUCTION

Earth-abundant semiconducting materials are attractive solutions in large-scale energy conversion and storage deployment.[1,2] There is a resurgence of interest in Zn−P compounds as promising materials for cost-effective and scalable thin-film PV applications[3−6] because their constituent elements are non-toxic, widely available, and more affordable alternatives to currently employed PV materials.[7] Among various Zn−P compounds, the tetragonal Zn$_3$P$_2$ has received particular attention owing to its suitable direct band gap of 1.5 eV,[8] high visible-light absorption and extinction coefficient ($>10^4$ cm^{-1}),[9,10] and long minority-carrier diffusion length ($\sim$10 μm).[11] Although the band gap energies of the monoclinic ZnP$_2$ member, reported in the range of 1.33−1.60 eV,[12−14] also fall within the values of the maximum absorption efficiency described by the Shockley−Queisser limit,[15−17] it has been largely overlooked as a candidate for PV applications. It has, however, been investigated and used as an anode material in Li-ion and Na-ion batteries, together with its tetragonal polymorph and Zn$_3$P$_2$ counterparts,[18−20] whereas ZnP$_2$ has been shown to outperform Zn$_3$P$_2$ in electrochemical performance for it has higher reversible capacity. In a recent density functional theory (DFT) study, we systematically characterized the mechanical, structural, and electronic properties of both tetragonal and monoclinic ZnP$_2$ and discussed their

implications for PV applications.[21] The spectroscopic limited maximum efficiency of monoclinic ZnP$_2$ was computed to be 10% for a reasonable reference thickness of 0.5 μm, demonstrating its promising potential as a photovoltaic material.

However, an inherent drawback of zinc-based semiconducting materials is their low surface stability in the presence of moisture and oxygen,[22−26] and efforts are now directed toward surface modification to aid their integration into photovoltaic devices and exploit their suitable optoelectronic properties. An important part of these investigations has focused on the modification of known inorganic semiconductor surfaces with organic molecules. Organic functionalization can enhance the surface stability against temperature and possible oxidation in the presence of oxygen and moisture that could result in material degradation. Protection strategies of zinc-based semiconductors (e.g. Zn−O,[27−29] Zn−S,[30−32] Zn$_3$P$_2$,[8,33]

Zn_3N_2,[34,35] $ZnSe$[36,37]) for photovoltaic applications, employing different surfactant molecules ranging from amines,[38] over acids[39] and thiols[40] to polymers,[41−43] have been developed and successfully applied in the laboratory. In addition, hybrid organic−inorganic nanostructures are of great interest because their optical and electrical properties can be efficiently tailored by surface functionalization. For example, surface modification of ZnO nanoparticles with pyrene-1-carboxylic acid showed an increase in the short-circuit current densities with lower open-circuit voltage, which was assigned to better carrier collection.[39] Furthermore, large-scale functionalization of Zn_3P_2 nanowires was achieved experimentally with two different ligand molecules, 4-aminothiophenol and 3-propane-dithiol. Both systems were found to be stable over 120 days without any agglomeration or degradation, thus providing a promising method for Zn_3P_2 passivation.[40] Based on these results, theoretical insight was reported on the adsorption strength and charge transfer between the 4-aminothiophenol and 3-propanedithiol and the Zn_3P_2 nanowires, which were represented by a (100) slab.[44] A more recent study focused on the functionalization of Zn_3P_2 nanocrystals with 4-amino-thiophenol and its influence on the electronic properties of varying surfaces of the material.[45] Different coupling schemes of available functional groups have been investigated, and inequivalent interacting modes were assigned as the most favorable for distinct Zn_3P_2 surfaces.

Despite extensive investigations on the functionalization of Zn_3P_2, no studies have been dedicated to the characterization of the interface chemistry between ZnP_2 and organic molecules, which makes this work timely. In the present study, a series of comprehensive DFT calculations were carried out, aimed at unraveling the mechanism of adsorption of 4-aminothiophenol on the low Miller index surfaces of monoclinic ZnP_2 and depicting the properties of the resulting hybrid structures. Atomic-level calculations based on DFT techniques have become powerful tools to describe organic−inorganic interfaces because they are capable of accurately predicting the lowest-energy adsorption geometries and identifying the charge transfer and other electronic effects.[46,47] As the 4-aminothiophenol has two functional groups (thiol (−SH) and amine (−NH_2) end group), different binding modes that involve one or both functional groups have been considered, and the energetics of the obtained adsorption configurations have been analyzed. Using predicted surface energies, the equilibrium morphologies of ZnP_2 nanocrystals before and after functionalization with 4-aminothiophenol were constructed according to the Wulff theorem. The results are expected to provide useful information about the interactions between ZnP_2 and organic molecules for future functionalization strategies and shape modulation of ZnP_2 nanoparticles.

2. COMPUTATION DETAILS

The spin-polarized Kohn−Sham DFT[48,49] calculations were carried out within the Vienna Ab-initio Simulation Package.[50] The exchange−correlation functional was approximated using the Perdew−Burke−Ernzerhof (PBE) parameterization of the generalized gradient approximation (GGA) for structural relaxations, whereas the hybrid HSE06 functional was employed for the calculation of electronic properties.[51] The projector augmented wave (PAW)[52,53] pseudo-potential method was imposed, and core electrons up to and including 3p for Zn, 2p for P and S, and 1s levels for N and O,

respectively, were kept frozen. The long-range dispersion interactions were added through the DFT-D3 method, as developed by Grimme et al.[54]

The kinetic energy cut-off of the wave functions was set to 500 eV, with bulk calculations carried out in the reciprocal space with a $5 \times 5 \times 5$ k-point mesh. The METADISE code[55] was employed to construct the surfaces, and final surface models were built as slabs of material with periodic boundary conditions, and a 20 Å vacuum was added in the direction orthogonal to the surface to prevent interaction between vertical images. Each surface slab is built of twelve atomic layers, comprising four ZnP−P−ZnP trilayers that each contain four ZnP_2 units, schematically represented for the (001) surface in Figure S1 of the Supporting Information. All atoms in the surface slab were allowed to relax, and a k-point mesh of $5 \times 5 \times 1$ was used for surface relaxations. The conjugate gradient technique, with total energy and force convergence criteria set at 10^{-6} eV and 0.01 eV/Å, respectively, has been used to perform structural optimizations.

Surface energies of relaxed bare slabs (γ) have been calculated as

$$\gamma = \frac{E_{\text{slab}}^{\text{DFT}} - n \times E_{\text{bulk}}^{\text{DFT}}}{2A_{\text{slab}}} \qquad (1)$$

where $E_{\text{slab}}^{\text{DFT}}$ and $E_{\text{bulk}}^{\text{DFT}}$ represent the DFT energies of the relaxed slab and bulk, respectively, A_{slab} is the surface area, and n is the ratio between the number of atoms in the slab and the number of atoms in the bulk. The electronic work function (ϕ), that is the energy required to withdraw an electron from the solid to the vacuum, was calculated as the difference between the vacuum electrostatic potential energy and the Fermi energy.

Adsorption of 4-aminothiophenol was carried out on the 2×1 [(011), (101), and (111)] and 2×2 [(001), (010), (100), and (110)] supercells of the ZnP_2 surfaces to minimize the lateral interactions between the adsorbate molecules. The k-point mesh was subsequently reduced to a gamma point only as the cell vectors reached lengths over 30 Å. Three initial adsorption modes were chosen: a single horizontal and two vertical geometries, one with the −SH and the other with the −NH_2 group facing the surface. No constraints on surface atoms or the adsorbing molecule were imposed during the optimization. In particular, the 4-aminothiophenol molecule was free to move laterally and vertically from its initial binding site or reorient itself to find the lowest-energy adsorption geometry. The strength of interaction between 4-amino-thiophenol and ZnP_2 surfaces was characterized by the adsorption energy (E_{ads}), calculated as

$$E_{\text{ads}} = E_{\text{surface+adsorbate}}^{\text{DFT}} - (E_{\text{surface}}^{\text{DFT}} + E_{\text{adsorbate}}^{\text{DFT}}) \qquad (2)$$

with $E_{\text{surface+adsorbate}}^{\text{DFT}}$, $E_{\text{surface}}^{\text{DFT}}$, and $E_{\text{adsorbate}}^{\text{DFT}}$ representing calculated energies of the surface with adsorbed 4-aminothiophenol, bare surface, and a 4-aminothiophenol molecule in a box, respectively. Negative E_{ads} indicates spontaneous adsorption of the molecule onto the surface with the most stable adsorption mode characterized by the most negative adsorption energy. The reference energy of a single adsorbate molecule was determined by optimizing it in a cubic box of 15 Å a side and sampling only over a gamma point.

Full coverage functionalization was carried out only for the most favorable adsorption mode, where the surface is considered to be fully functional once all the zinc atoms on
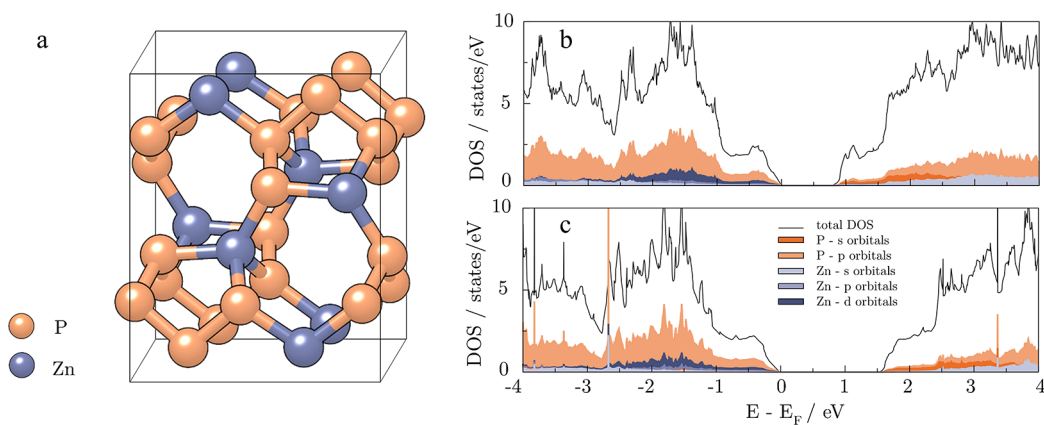
Figure 1. Optimized structure of bulk monoclinic ZnP$_2$ (a) and its orbital-decomposed DOS computed with the GGA (PBE) (b) and HSE06 (c) functionals.
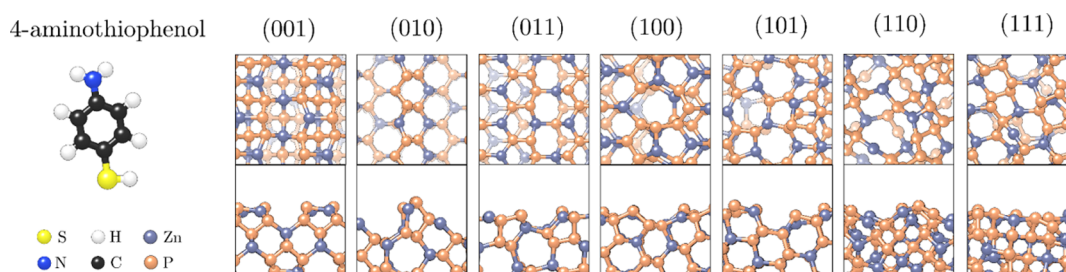

Figure 2. Optimized structures of 4-aminothiophenol (leftmost) and seven low-Miller index surfaces of monoclinic ZnP$_2$ in top and side views. To create a depth perception, the topmost surface atoms have been represented with more vivid colors.

the surface are unavailable for further adsorption. Surface energies after functionalization (γ_f) were determined as

$$\gamma_f = \frac{E_{\text{func surface}}^{\text{DFT}} - (n \times E_{\text{bulk}}^{\text{DFT}} + m \times E_{\text{adsorbate}}^{\text{DFT}})}{2A_{\text{slab}}} \quad (3)$$

where $E_{\text{func surface}}^{\text{DFT}}$ is the calculated energy of the surface functionalized by a full monolayer, and m is the number of adsorbed 4-aminothiophenol molecules. Calculated surface energies were subsequently employed to obtain Wulff morphologies,[56] as implemented in the Wulffmaker[57] software.

3. RESULTS AND DISCUSSION

3.1. Bulk and Surface Characterization of ZnP$_2$. The monoclinic ZnP$_2$ bulk structure (Figure 1a), optimized at the GGA level, has lattice parameters of a = 8.611 Å, b = 7.239 Å, and c = 7.530 Å, which agree well with the available experimental data[12] of a = 8.863 Å, b = 7.288 Å, and c = 7.560 Å, respectively. In our previous study,[21] we found that the standard GGA significantly underestimated the electronic band gap of monoclinic ZnP$_2$, with the calculated value of 0.76 eV being only half the experimental band gap, reported in the range of 1.33−1.60 eV.[13,58−60] To resolve this deficiency, the hybrid HSE06 functional was employed, yielding an electronic band gap of 1.46 eV, in good agreement with experimental data. The orbital-decomposed densities of state (DOS) computed with the GGA (PBE) and HSE06 functionals are shown in Figure 1b,c.

From the optimized bulk structure, the seven low-Miller index surfaces were cut and relaxed by GGA in order to determine their optimal arrangements and stabilities. Shown in Figure 2 are the optimized structures of the most stable terminations of the seven surfaces, with the calculated

unrelaxed and relaxed surface energies reported in Table 1. According to the calculated percentage relaxations, all surfaces

Table 1. Calculated Surface Energies [Unrelaxed (γ_u) and Relaxed (γ_r)], Percentage Relaxation, and Work Functions (ϕ) of the Most Stable Terminations of the Seven Low Miller Index ZnP$_2$ Surfaces

surface	termination	γ_u/J m^{-2}	γ_r/J m^{-2}	relaxation/%	ϕ/eV
(001)	−Zn−Zn−	1.006	0.728	−27.63	4.614
(010)	−P−P−	1.278	0.949	−25.74	4.561
(011)	−Zn−	1.001	0.739	−26.17	4.245
(100)	−P−Zn−	1.514	0.889	−41.28	4.429
(101)	−P−P−	1.165	0.899	−22.83	4.382
(110)	−P−	1.699	1.028	−39.49	4.402
(111)	−Zn−	1.364	0.985	−27.79	4.139

undergo significant adjustments to reach the most stable configuration. The relaxed surfaces exhibit similar stabilities, as reflected in the small differences in their final surface energies. The (001) and (011) surfaces are predicted as the most stable with surface energies of 0.728 and 0.739 J m^{-2}, respectively. They are followed by the (100) and (101) surfaces whose calculated surface energies are 0.889 and 0.899 J m^{-2}, respectively. With surface energies of 0.949, 1.028, and 0.985 J m^{-2}, the (010), (110), and (111) surfaces are predicted to be less favorable, suggesting that the (110) surface is the least stable low-Miller index surface of monoclinic ZnP$_2$. Considering that all surfaces have similar stabilities and are hence likely to be expressed in the nanocrystal structure of ZnP$_2$, the adsorption of 4-aminothiophenol (Figure 2, leftmost) was investigated on each surface to compare the nanocrystal morphologies before and after functionalization.

3.2. Single 4-Aminothiophenol Adsorption on ZnP$_2$ Surfaces. To determine the preferred binding modes of the 4-aminothiophenol molecule on various low-Miller index surfaces of ZnP$_2$, several different initial adsorption orientations were optimized without any symmetry constraints.

3.2.1. ZnP$_2$ (001) Surface. At the ZnP$_2$ (001) surface, 4-aminothiophenol binds in three possible modes, as shown in Figure 3. The calculated adsorption energies, interatomic bond
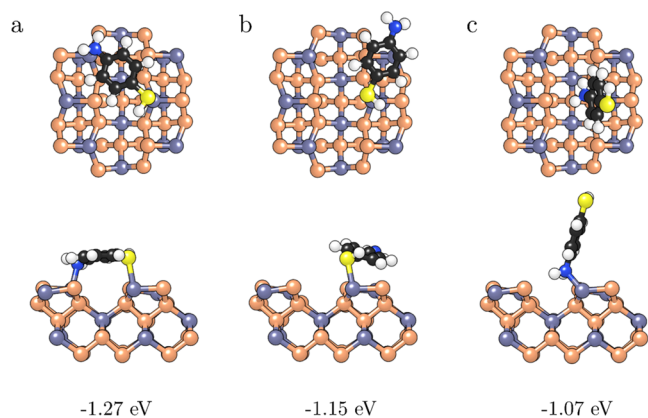

-1.27 eV   -1.15 eV   -1.07 eV

Figure 3. Top (top panel) and side views (bottom panel) of the horizontal (a), −SH vertical (b), and −NH$_2$ vertical (c) adsorption modes of 4-aminothiophenol on the ZnP$_2$ (001) surface. For clarity, only the topmost layers of the surface are shown. Calculated adsorption energies are listed below each structure. For color legend, refer to Figure 2.

distances, and charge transfers are summarized in Table 2. The most stable binding mode is predicted to be a bidentate geometry (Figure 3a), wherein the 4-aminothiophenol molecule gets adsorbed parallel to the surface forming both N−Zn (2.26 Å) and S−Zn (2.64 Å) bonds. This structure

released an adsorption energy of −1.27 eV. Two vertical monodentate configurations, one binding through the sulfur of the thiol group (Figure 3b) and the other through the nitrogen of the amino group (Figure 3c), relaxed to differently slanted structures. Binding of 4-aminothiophenol through the thiol group resulted in repositioning horizontally toward the surface, with an angle between the N−S vector and a plane of the surface (Figure S2 of the Supporting Information) of 7.30° and a shorter S−Zn bond of 2.57 Å compared to the same bond of the bidentate interaction mode. When interacting solely through the −NH$_2$ group, the 4-aminothiophenol molecule remains vertically oriented with an angle of 73.89° and a N−Zn distance of 2.17 Å, which is also shorter than when adsorbed as a bidentate. However, the adsorption energies of both monodentate modes show weaker interaction and are calculated to be E_{ads} = −1.15 and E_{ads} = −1.07 eV for −SH and −NH$_2$ interacting groups, respectively.

Regardless of the interaction mode of adsorption, the molecule of 4-aminothiophenol gained an electronic charge upon binding to the ZnP$_2$ (001) surface. The amount of charge gained through a single Zn−N bond in the -NH$_s$ vertical binding mode, namely −0.06 e$^-$, is only half of what is transferred in the horizontal or −SH vertical mode (−0.14 and −0.13 e$^-$, respectively). However, the zinc atom directly involved in the adsorption of the molecule through the −NH$_s$ group loses more than double the charge contained within the adsorbate. The remaining negative charge is traced to the topmost neighboring phosphorus atom (−0.06 e$^-$) connected to the interacting zinc. All structural and electronic parameters are listed in Table 2, while distribution of the gained charge over atoms of the 4-aminothiophenol molecule can be found in Table S1, Supporting Information.

3.2.2. ZnP$_2$ (010) Surface. The optimized binding modes of 4-aminothiophenol on the ZnP$_2$ (010) surface are presented in Figure 4. The channel-like structure of this surface, as indicated

Table 2. Adsorption Energies (E_{ads}), Bond Lengths (d), Angles between the N−S Vector and a Surface Plane (θ), and Changes in the Bader Charge (Δq) Upon the Adsorption of a Single 4-Aminothiophenol Molecule on Low-Miller Index Surfaces of Monoclinic ZnP$_2$[a]

surface	binding mode	E_{ads}/eV	d (S−Zn)/Å	d (N−Zn)/Å	θ/deg	Δq (adsorbate)/e$^-$	Δq (Zn$_S$)/e$^-$	Δq (Zn$_N$)/e$^-$
(001)	horizontal	−1.27	2.64	2.26		−0.14	0.02	0.06
	−SH vertical	−1.15	2.57		7.30	−0.13	0.01	
	−NH$_2$ vertical	−1.07		2.17	73.89	−0.06		0.10
(010)	horizontal	−2.04	2.70	2.26		−0.06	0.01	0.08
	−SH vertical	−1.47	2.52		74.75	−0.07	0.02	
	−NH$_2$ vertical	−0.98	2.18		69.82	−0.09		0.11
(011)	horizontal	−1.65	2.83	2.31		−0.09	0.02	0.06
	−SH vertical	−1.08	2.47		88.19	−0.11	0.03	
	−NH$_2$ vertical	−0.92		2.18	28.30	−0.08		0.09
(100)	horizontal	−1.47	2.56	2.36		−0.11	0.00	0.04
	−SH vertical	−1.33	2.50		10.00	−0.12	0.02	
	−NH$_2$ vertical	−0.78		2.19	80.05	−0.08		0.09
(101)	horizontal	−1.91	2.54	2.17		−0.16	0.03	0.09
	−SH vertical	−0.79	2.53		86.90	−0.08	0.03	
	−NH$_2$ vertical	−1.17		2.17	70.51	−0.08		0.07
(110)	horizontal	−1.38	2.45	(4.31)		−0.06	0.02	
(111)	horizontal	−1.41	2.52	(3.89)		−0.13	0.06	0.01
	−SH vertical	−0.82	2.58		32.72	−0.11	0.07	
	−NH$_2$ vertical	−1.23	2.15	2.15	60.48	−0.09		0.13

[a]Structural parameters are obtained through the relaxation with the GGA (PBE) exchange functional, while HSE06 was used to calculate Bader charges. Negative changes in the Bader charge represent a gain in the electronic charge, while positive changes represent a loss of electrons.
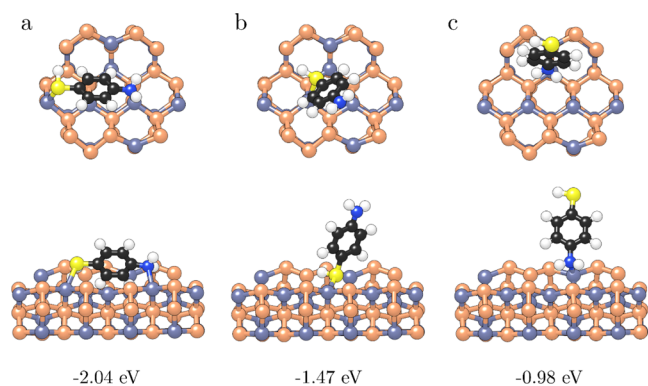
Figure 4. Top (top panel) and side views (bottom panel) of horizontal (a), −SH vertical (b), and −NH$_2$ vertical (c) adsorption modes of 4-aminothiophenol on ZnP$_2$ (010). For clarity, only the topmost layers of the surface are shown. Calculated adsorption energies are listed below each structure. For color legend, refer to Figure 2.
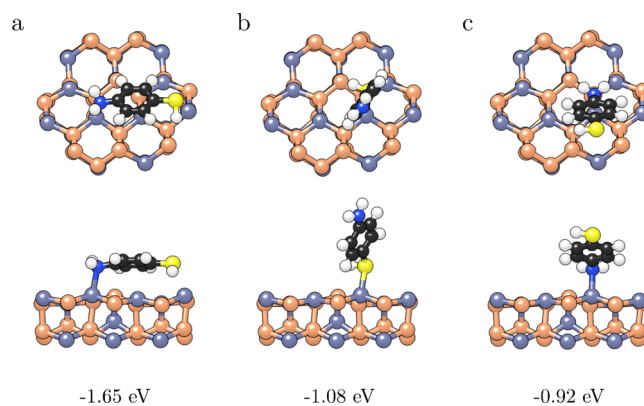

Figure 5. Top (top panel) and side views (bottom panel) of horizontal (a), −SH vertical (b), and −NH$_2$ vertical (c) adsorption modes of 4-aminothiophenol on the ZnP$_2$ (011) surface. For clarity, only the topmost layers of the surface are shown. Calculated adsorption energies are listed below each structure. For color legend, refer to Figure 2.

in Figure 2, can accommodate the 4-aminothiophenol molecule horizontally inside the channel, allowing for a relatively strong bidentate interaction (Figure 4a) with an adsorption energy of E_{ads} = −2.04 eV. Established S−Zn and N−Zn bonds have lengths of 2.70 and 2.26 Å, respectively, and the whole molecule gains a charge of −0.056 e$^−$, mostly from the zinc atom interacting with the −NH$_2$ functional group. When adsorbed vertically through the −SH functional group (Figure 4b), sulfur binds to the Zn atom situated inside the surface channel (2.52 Å Zn−S bond), releasing an adsorption energy of −1.47 eV, with −0.068 e$^−$ of the charge transferred to the adsorbate. When adsorbed via the amine nitrogen in a vertical monodentate geometry (Figure 4c), the bulkiness of the −NH$_2$ functional group prevents adsorption directly inside the channel and the N atom binds to an outer zinc atom instead (2.18 Å Zn−N bond). Without further interactions between the rest of the molecule and the ZnP$_2$ (010) surface, the −NH$_2$ vertical binding mode released an adsorption energy of −0.98 eV, which is only half as favorable as the bidentate interaction. However, in this mode, 4-aminothiophenol acquires the highest amount of charge from the surface, −0.086 e$^−$.

3.2.3. ZnP$_2$ (011) Surface. The optimized structures of the three binding modes of 4-aminothiophenol on the ZnP$_2$ (011) surface and their adsorption energies are shown in Figure 5. The horizontal positioning of 4-aminothiophenol resulted in an interaction very close to that of a bidentate binding mode (Figure 5a), with a Zn−N bond of 2.31 Å and a distance between the −SH sulfur atom and the closest surface zinc atom of 2.83 Å. Despite the prolonged Zn−S distance, this type of interaction is characterized by an adsorption energy of E_{ads} = −1.65 eV, which is more favorable by 0.57 and 0.73 eV, respectively, than the −SH (Figure 5b) and −NH$_2$ (Figure 5c) monodentate vertical binding modes. When interacting only through the −SH functional group, the adsorbate binds almost perpendicularly to the surface with the Zn−S bond optimized at 2.47 Å. In the−NH$_2$ binding mode (Zn−N bond of 2.17 Å), the molecule is tilted much closer to the surface at an angle of 28.30°. Transfer of negative charge to 4-aminothiophenol is the highest in the case of monodentate interaction through the sulfur atom, −0.11 e$^−$, and the lowest for the opposite case of interacting solely through the amino group, −0.08 e$^−$.

3.2.4. ZnP$_2$ (100) Surface. The three binding modes of 4-aminothiophenol on the ZnP$_2$ (100) surface, together with their corresponding adsorption energies, are presented in Figure 6. Zn−S and Zn−N bonds formed in the horizontal
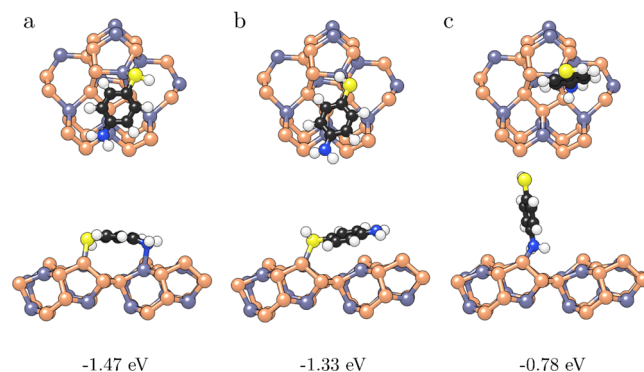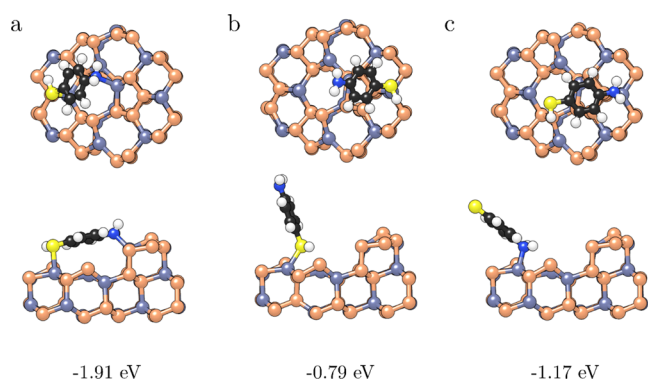

Figure 6. Top (top panel) and side views (bottom panel) of horizontal (a), −SH vertical (b), and −NH$_2$ vertical (c) adsorption modes of 4-aminothiophenol on the ZnP$_2$ (100) surface. For clarity, only the topmost layers of the surface are shown. Calculated adsorption energies are listed below each structure. For color legend, refer to Figure 2.

bidentate mode (Figure 6a) have lengths of 2.56 and 2.36 Å, respectively, and release an adsorption energy of −1.47 eV. For the −SH monodentate binding geometry (Figure 6b), the 4-aminothiophenol molecule is tilted toward the surface at an angle of 10.00°, forming a Zn−S bond of 2.50 Å with the thiol hydrogen pointing away from the surface. This adsorption geometry is only 0.15 eV less favorable than the bidentate binding mode. In contrast, when the molecule is adsorbed in a monodentate mode through the amino group with a rather shorter 2.17 Å Zn−N bond, it remains almost perfectly perpendicular (Figure 6c). However, this binding mode is also significantly less favorable with an adsorption energy of E_{ads} = −0.78 eV.

The charges gained through the adsorption process are similar for horizontal and −SH vertical interaction modes, −0.11 and −0.12 e$^−$, respectively. However, the amount of negative charge transferred from the zinc atom bound to sulfur

is 0.02 e$^-$ for the −SH monodentate binding mode, which is ten times that of the bidentate interaction, where the charge gained (0.002 e$^-$) is almost negligible, and the majority of the charge transfer comes from Zn interacting with the −NH$_2$ group, 0.04 e$^-$. Correspondingly, a significant change of 0.088 e$^-$ is observed in the charge of the zinc atom interacting to form an amine monodentate, leading to a net charge gain of −0.08 e$^-$ by 4-aminothiophenol.

3.2.5. ZnP$_2$ (101) Surface. The structures and adsorption energies of the distinct adsorption modes of 4-aminothiophenol on the ZnP$_2$ (101) surface are presented in Figure 7. The (101) surface has a naturally stepped geometry which

-1.91 eV   -0.79 eV   -1.17 eV

Figure 7. Top (top panel) and side views (bottom panel) of horizontal (a), −SH vertical (b), and −NH$_2$ vertical (c) adsorption modes of 4-aminothiophenol on the ZnP$_2$ (101) surface. For clarity, only the topmost layers of the surface are shown. Calculated adsorption energies are listed below each structure. For color legend, refer to Figure 2.

allows for efficient adsorption in the bidentate binding mode (Figure 7a), as seen in its adsorption energy of E_{ads} = −1.91 eV, the most favorable of the three adsorption modes. This is also reflected in the lengths of formed S−Zn and N−Zn bonds of 2.54 and 2.17 Å, respectively. Compared to the bidentate binding, the monodentate −SH (Figure 7b) and −NH$_2$ (Figure 7c) geometries released adsorption energies of −0.79 and −1.17 eV, respectively, with tilting angles of 86.90 and 70.51°, and Zn−S and Zn−N bonds converged at 2.53 and 2.17 Å, respectively. The charge gained in the most stable horizontal bidentate adsorption geometry on the (101) surface is −0.15 e$^-$ with the zinc atom binding the nitrogen, contributing three times more to the charge transfer compared to the zinc atom connected to the −SH sulfur. 4-aminothiophenol gained a charge of −0.08 e$^-$ when adsorbed in both −SH and −NH$_2$ monodentate geometries.

3.2.6. ZnP$_2$ (110) Surface. Only one binding mode was successfully optimized on the ZnP$_2$ (110) surface, and its structure is depicted in Figure 8. The zigzag arrangement of surface zinc atoms and their interatomic distance hamper the 4-aminothiophenol molecule from forming a bidentate geometry with one S−Zn and one N−Zn bond. The molecule hence binds to the surface through a single S−Zn bond instead, with an adsorption energy of E_{ads} = −1.38 eV and a charge transfer of −0.06 e$^-$.

3.2.7. ZnP$_2$ (111) Surface. 4-aminothiophenol binds to the (111) surface in two monodentate −SH geometries, horizontal (Figure 9a) and tilted (Figure 9b). The horizontal binding mode is characterized by the stronger adsorption energy of E_{ads} = −1.41 eV, compared to E_{ads} = −0.82 eV for the tilted mode.
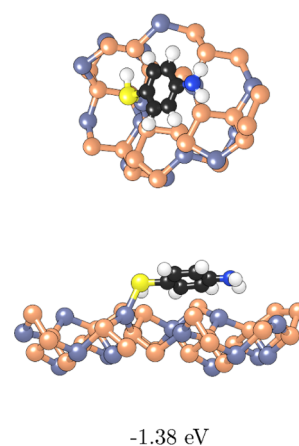

-1.38 eV

Figure 8. Top (top panel) and side views (bottom panel) of horizontal adsorption mode of 4-aminothiophenol on the ZnP$_2$ (110) surface. For clarity, only the topmost layers of the surface are shown. The calculated adsorption energy is also given. For color legend, refer to Figure 2.
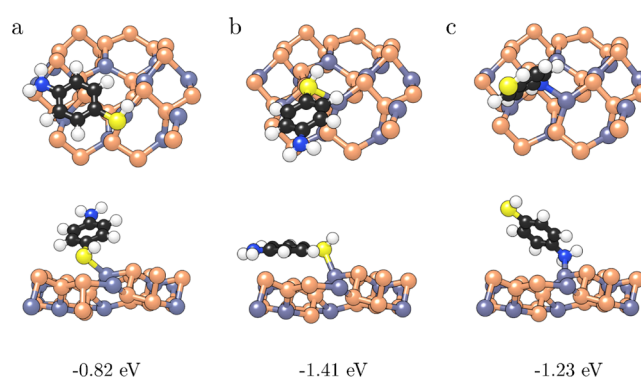

-0.82 eV   -1.41 eV   -1.23 eV

Figure 9. Top (top panel) and side views (bottom panel) of −SH horizontal (a), −SH vertical (b), and −NH$_2$ vertical (c) adsorption modes of 4-aminothiophenol on the ZnP$_2$ (111) surface. For clarity, only the topmost layers of the surface are shown. Calculated adsorption energies are listed below each structure. For color legend, refer to Figure 2.

A true bidentate mode could not be established, even when positioning the molecule parallel to the surface, due to the inconvenient arrangement of topmost Zn atoms. In the horizontal −SH geometry, the Zn−S bond has a length of 2.52 Å, while the distance between the nitrogen and the nearest zinc surface atom is 3.89 Å. The Zn−S bond distance in the tilted −SH monodentate geometry is predicted at 2.58 Å with a tilt angle of 32.72°. The monodentate −NH$_2$ vertical binding mode (Figure 9c), established through the 2.15 Å Zn−N bond, is only 0.18 eV less favorable than when 4-aminothiophenol is adsorbed in the horizontal −SH geometry, and it releases an adsorption energy of −1.23 eV. Overall, 4-aminothiophenol gains a charge of −0.13 e$^-$ and −0.11 e$^-$ when adsorbed in the horizontal and tilted −SH geometries, respectively, and −0.09 e$^-$ when binding through the −NH$_2$ group.

3.3. Functionalization at Full Coverage of the ZnP$_2$ Surfaces. Full-coverage functionalization of ZnP$_2$ surfaces was investigated by considering multiple 4-aminothiophenol molecules adsorbed in the horizontal binding mode, which was shown to be the most favorable type of interaction on all surfaces. Each surface was functionalized with a full monolayer

of 4-aminothiophenol, where the monolayer coverage had been established when no combination of uncoordinated zinc atoms remained available to accommodate another adsorbate molecule in a flat bidentate binding mode. The calculated adsorption energies at full coverage are reported in Table 3,

Table 3. Adsorption Energy per Molecule for the Horizontal Binding Mode ($\overline{E}_{ads}$), Surface Energy (γ_f), Percentage Stabilization, and Work Function (ϕ_f) for Seven Low-Miller Index Surfaces of Monoclinic ZnP_2 Upon a Full Monolayer Functionalization with 4-Aminothiophenol

surface	$\overline{E}_{ads}$/eV	γ_f/J m^{-2}	stabilization/%	ϕ_f/eV
(001)	−1.13	0.678	−6.8	4.207
(010)	−2.10	0.881	−7.1	3.816
(011)	−1.65	0.722	−2.3	3.927
(100)	−1.44	0.853	−4.0	4.924
(101)	−1.90	0.770	−14.4	4.269
(110)	−1.51	0.898	−12.6	4.837
(111)	−1.40	0.883	−10.3	3.057

with the strength of adsorption predicted to follow the trend (010) > (101) > (011) > (110) > (100) > (111) > (001). Using the full-coverage energetics, the surface energies and work functions of the functionalized surfaces were also calculated and are listed in Table 3.

To determine the effect of the functionalization on the electronic properties of ZnP_2 surfaces, changes in the decomposed DOS and band gap energies upon adsorption have been examined. Orbital-decomposed DOS of the (001) surface before and after full monolayer functionalization are shown in Figure 10. Similar to the DOS of the bulk material, the top of the valence band of the (001) surface is dominated by p states of phosphorus and p and d states of zinc, while the bottom of the conduction band is composed mainly of the s states of P atoms and p states of Zn atoms.

The adsorption of 4-aminothiophenol is shown to be characterized by the Zn−S and Zn−N bonding states localized at around −3.0 eV below the Fermi level. The electronic band gaps of the naked and functionalized (001) surfaces are

calculated at 0.936 and 0.924 eV, respectively, indicating that the functionalization with 4-aminothiophenol has only a negligible effect on the electronic structure. The composition of the valence and conduction band edges of the functionalized surface remained unchanged, and no additional states were introduced in close proximity or within the energy gap. The corresponding figures of the orbital-decomposed DOS for the remaining six surfaces can be found in the Supporting Information, Figures S3 and S4, where no significant effects of the adsorbate monolayers on the electronic properties were observed, and band gap energies of the functionalized surfaces remained within 0.005−0.100 eV of their naked counterparts.

3.4. Morphology of the ZnP_2 Nanocrystal before and after 4-Aminothiophenol Functionalization. Modifications in the shape of the ZnP_2 nanocrystal after 4-aminothiophenol functionalization were ascertained through the Wulff construction,[56] based on the surface energies of the clean and monolayer-protected surfaces, Figure 11. Under thermo-
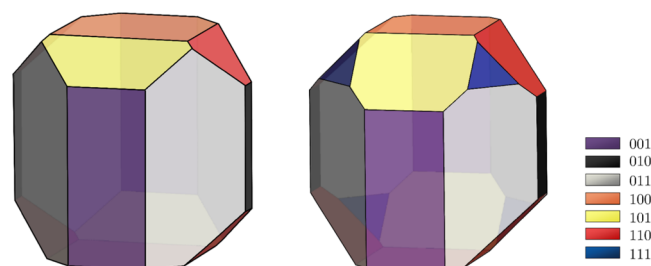

Figure 11. Wulff morphology of the bare (left) and 4-aminothiophenol-functionalized (right) monoclinic ZnP_2 crystal.

dynamic conditions, the equilibrium morphology of a crystal possesses minimal total surface free energy for a given volume based on the Gibbs formulation. Functionalization is demonstrated to have a stabilizing effect on all ZnP_2 surfaces, as reflected in the lower surface energies, with the extent of the stabilization varying from 2.3% for the (011) surface up to 14.4% for the (101) surface.
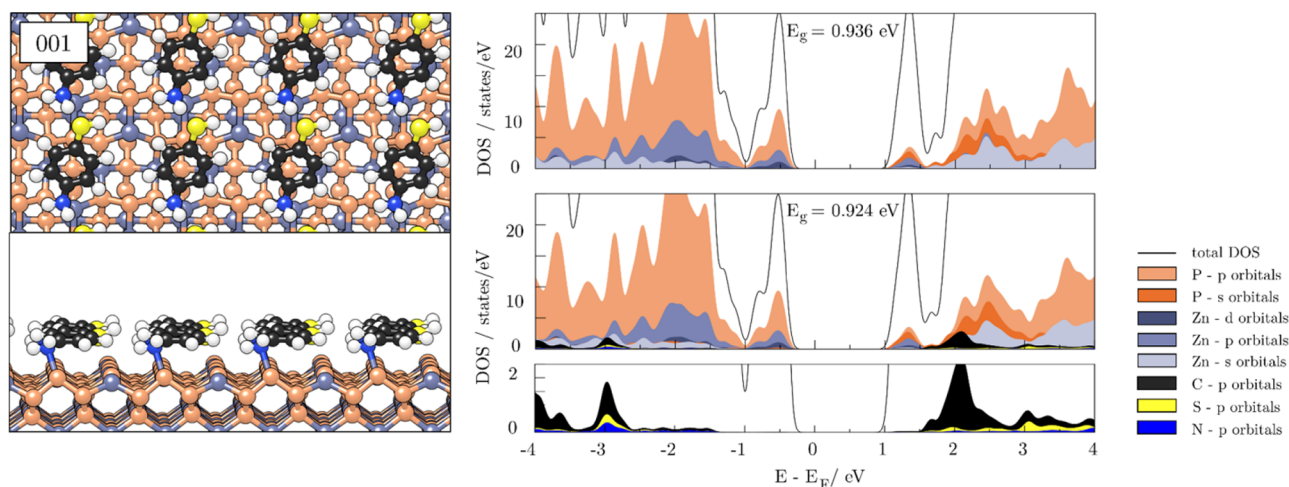

Figure 10. Left: the (001) surface of monoclinic ZnP_2 functionalized with a full monolayer of 4-aminothiophenol in the horizontal binding mode in top view (top panel) and side view (bottom panel). Right: orbital-decomposed DOS of the bare (001) surface of monoclinic ZnP_2 with an accompanying band gap energy, E_g (top panel); orbital-decomposed DOS of the functionalized (001) surface of monoclinic ZnP_2 presented on the left with an accompanying band gap energy, E_g (middle panel); enlarged DOS of the atoms of 4-aminothiophenol after monolayer functionalization of the (001) surface of monoclinic ZnP_2 (bottom panel).
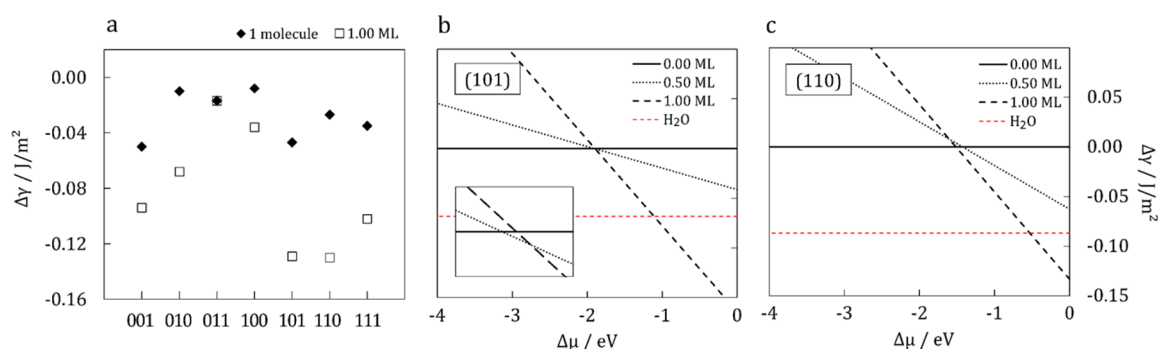
Figure 12. (a) Surface free energy variations for seven low-Miller index surfaces of monoclinic ZnP_2 functionalized with a single molecule of 4-aminothiophenol and a full monolayer under adsorbate-rich conditions (μ_a = 0.00 eV). Surface phase diagrams of the (101) surface (b) with an enlarged area of intersection, and of the (110) surface, (c). y-axis is the same for the two surface phase diagrams.

Adsorption-induced changes in the surface energies are also visible in the final morphology of the ZnP_2 nanoparticle. Prior to the functionalization, the equilibrium shape of the bare crystal contains six out of the seven surfaces studied, with the (111) surface not appearing in the morphology. The (001) and (011) surfaces account for the greatest share of the surface area, in agreement with their favorable surface stabilities among the seven surfaces investigated. Differences in the adsorption strength of 4-aminothiophenol on the seven surfaces influence their stabilities and, hence, their expression in the morphology of the functionalized nanoparticle. The weaker adsorption on the (001) and (100) surfaces compared to the others results in a reduction of their surface shares, whereas the (101) and (110) surfaces experience an increase in their share of the available surface area, resulting from higher stabilization from 4-aminothiophenol adsorption. Owing to the stabilization of the (111) surface after functionalization, it now appears in the final equilibrium morphology.

3.5. Thermodynamic Stability of Functionalized ZnP_2 Surfaces. Calculated adsorption energies are good descriptors of the strength of interaction between 4-aminothiophenol and various ZnP_2 surfaces, but they do not give any indication of the effects of experimental conditions and chemical potential of the adsorbate on the stability of functionalized surfaces. Stabilities of the surfaces upon functionalization were therefore estimated and compared based on the change in the free Gibbs surface energy with respect to the conditions of temperature and pressure ($\Delta\gamma_f(T,p)$) as

$$\Delta\gamma_f(T, p) = \frac{E_{\text{funct surface}}^{\text{DFT}} - E_{\text{surface}}^{\text{DFT}}}{2A} - \frac{m}{2A}\Delta\mu_a(T, p)$$

where $\Delta\mu_a(T,p)$ is the variation of the chemical potential of 4-aminothiophenol to account for experimental conditions. Assuming adsorbate-rich conditions (corresponding to $\Delta\mu_a(T,p) = 0$, when the chemical potential of 4-aminothiophenol equals the total energy of the molecule in the gas phase), the calculated changes in the Gibbs free surface energies are represented in Figure 12a. All surfaces undergo full monolayer functionalization under these conditions, with the most significant change in the Gibbs surface free energy noted for the (101) and (110) surfaces.

To fully capture the behavior of the surfaces under various conditions of adsorbate concentrations, surface phase diagrams have been suggested based on the changes in the Gibbs free surface energies with the chemical potential of 4-amino-thiophenol. The phase diagrams were plotted for the two most

stable functionalized surfaces, (101) and (110), as shown in Figures 12b,c, respectively. The two surfaces show similar trends, with the monolayer coverage favored up to the chemical potential of −1.50 and −2.00 eV. A transition to the lower coverage of 0.50 ML occurs at $\Delta\mu_a = -1.89$ eV for the (101) surface, while the appearance of the bare surface should occur shortly after, at $\Delta\mu_a = -1.91$ eV, which is shown in the enlarged area of the plot.

Conversely, an immediate transition to a bare surface is observed at $\Delta\mu_a = -1.51$ eV for the (110) surface without the appearance of the surface with half a monolayer of 4-aminothiophenol. The crossovers between high and low coverages (or, in most cases, bare surfaces) of all seven surfaces occur in the range of −1.50 to −2.00 eV; the only exception is the (001) surface where the intersection happens at $\Delta\mu_a = -1.12$ eV. If standard conditions are considered (p = 1 atm, T = 300 K), those transitions can be assigned to environments with extremely low adsorbate concentrations, $p \sim 10^{-15}$ to 10^{-17} atm for the six surfaces or $p \sim 10^{-10}$ atm for the (001) surface (note: ultra-high vacuum chambers operate at about 10^{-12} atm).

The effect of humidity was introduced by adding the variation of surface energies with adsorbed water. A previous study has shown spontaneous interaction of water molecules with all ZnP_2 surfaces,[61] and the calculated surface energies after full water monolayer adsorption under p = 1 atm (p_{H_2O} = 0.035 atm) and T = 300 K have also been provided in the phase diagrams (red dashed lines). It has to be noted that only the lowest chemical potential of water needed for the formation of the full monolayer was considered, and the true surface energy could hence be even lower. The transition from 1.00 ML of 4-aminothiophenol to 1.00 ML of water takes place depending on the surface, but it always occurs at much higher chemical potentials of 4-aminothiophenol compared to the transitions toward non-functionalized surfaces. For the surfaces whose phase diagrams are depicted in Figure 12, transitions are observed at $\Delta\mu_a = -0.82$ eV for the (101) surface and $\Delta\mu_a = -1.08$ eV for the (110) surface, which corresponds to the partial pressures of $p \sim 10^{-6}$ to 10^{-9} atm. Further estimation of the stability of the functionalized surfaces under more realistic aqueous media is not plausible solely from DFT calculations, but the provided results are suggestive of the possible protection of ZnP_2 nanoparticles under humid conditions by 4-aminothiophenol functionalization.

4. CONCLUSIONS

DFT calculations have been carried out to provide detailed atomic-level insights into the effects of the functionalization by 4-aminothiophenol on the structural and electronic properties of monoclinic ZnP_2 nanoparticles. The strongest interaction between the 4-aminothiophenol and all the ZnP_2 surfaces was established when the molecule was located close to the surface in a horizontal position. When the arrangement of the topmost zinc atoms was favorable, it provided an adsorption site which allowed both the $-NH_2$ and $-SH$ functional groups to form covalent bonds with the surface. The analysis of electronic structures of the surfaces functionalized by a full monolayer revealed minimal changes in the band gap energies, without new states in the band gap region, although changes in the morphology of the nanocrystals were much more prominent. Thermodynamically, the surfaces were found to be significantly stabilized after functionalization, with full monolayer coverages favored under adsorbate-rich conditions and expected to persist even in the presence of water, although it remains to see if in aqueous media this improvement in the stability remains sufficient to overcome the formation of a water monolayer. However, minimal modifications of the optically favorable band gap energies and adsorption strengths comparable to those observed at Zn_3P_2 surfaces indicate that 4-amino-thiophenol is a promising candidate for the functionalization of monoclinic ZnP_2 nanoparticles and thin films for photovoltaic applications.

■ ASSOCIATED CONTENT

Ⓢ Supporting Information

The Supporting Information is available free of charge at https://pubs.acs.org/doi/10.1021/acsaem.1c03804.

Adsorption structures, Bader charge analysis, and the orbital-decomposed DOS of the monoclinic ZnP_2 surfaces with and without a full monolayer functionalization with 4-aminothiophenol (PDF)

■ AUTHOR INFORMATION

Corresponding Author

Nelson Y. Dzade − *School of Chemistry, Cardiff University, CF10 3AT Cardiff, U.K.; John and Willie Leone Family Department of Energy and Mineral Engineering, The Pennsylvania State University, University Park, Pennsylvania 16802, United States;* ● orcid.org/0000-0001-7733-9473; Email: nxd5313@psu.edu

Authors

Barbara Farkaš − *School of Chemistry, Cardiff University, CF10 3AT Cardiff, U.K.;* ● orcid.org/0000-0002-8297-1673

Aleksandar Živković − *School of Chemistry, Cardiff University, CF10 3AT Cardiff, U.K.; Department of Earth Sciences, Utrecht University, 3548 CB Utrecht, The Netherlands;* ● orcid.org/0000-0003-1347-6203

Veikko Uahengo − *Department of Chemistry and Biochemistry, University of Namibia, Windhoek 9000, Namibia*

Nora H. de Leeuw − *School of Chemistry, Cardiff University, CF10 3AT Cardiff, U.K.; Department of Earth Sciences, Utrecht University, 3548 CB Utrecht, The Netherlands; School of Chemistry, University of Leeds, Leeds LS2 9JT, U.K.;* ● orcid.org/0000-0002-8271-0545

Complete contact information is available at: https://pubs.acs.org/10.1021/acsaem.1c03804

Notes

■ ACKNOWLEDGMENTS

■ REFERENCES

(1) Afzaal, M.; O'Brien, P. Recent Developments in II-VI and III-VI Semiconductors and Their Applications in Solar Cells. *J. Mater. Chem.* **2006**, *16*, 1597−1602.

(2) Garland, J. W.; Biegala, T.; Carmody, M.; Gilmore, C.; Sivananthan, S. Next-Generation Multijunction Solar Cells: The Promise of II-VI Materials. *J. Appl. Phys.* **2011**, *109*, 102423.

(3) Escobar Steinvall, S.; Tappy, N.; Ghasemi, M.; Zamani, R. R.; Lagrange, T.; Stutz, E. Z.; Leran, J.-B.; Zamani, M.; Paul, R.; Fontcuberta I Morral, A. Multiple Morphologies and Functionality of Nanowires Made from Earth-Abundant Zinc Phosphide. *Nanoscale Horiz.* **2020**, *5*, 274−282.

(4) Swain, R. A.; McVey, B. F. P.; Virieux, H.; Ferrari, F.; Tison, Y.; Martinez, H.; Chaudret, B.; Nayral, C.; Delpech, F. Sustainable Quantum Dot Chemistry: Effects of Precursor, Solvent, and Surface Chemistry on the Synthesis of Zn_3P_2 Nanocrystals. *Chem. Commun.* **2020**, *56*, 3321−3324.

(5) Paul, R.; Humblot, N.; Steinvall, S. E.; Stutz, E. Z.; Joglekar, S. S.; Leran, J.-B.; Zamani, M.; Cayron, C.; Logé, R.; del Aguila, A. G.; Xiong, Q.; Morral, A. F. i. Van Der Waals Epitaxy of Earth-Abundant Zn_3P_2 on Graphene for Photovoltaics. *Cryst. Growth Des.* **2020**, *20*, 3816−3825.

(6) Dzade, N. Y. Unravelling the Early Oxidation Mechanism of Zinc Phosphide (Zn_3P_2) Surfaces by Adsorbed Oxygen and Water: A First-Principles DFT-D3 Investigation. *Phys. Chem. Chem. Phys.* **2020**, *22*, 1444−1456.

(7) Wadia, C.; Alivisatos, A. P.; Kammen, D. M. Materials Availability Expands the Opportunity for Large-Scale Photovoltaics Deployment. *Environ. Sci. Technol.* **2009**, *43*, 2072−2077.

(8) Fagen, E. A. Optical Properties of Zn_3P_2. *J. Appl. Phys.* **1979**, *50*, 6505−6515.

(9) Kimball, G. M.; Müller, A. M.; Lewis, N. S.; Atwater, H. A. Photoluminescence-Based Measurements of the Energy Gap and Diffusion Length of Zn_3P_2. *Appl. Phys. Lett.* **2009**, *95*, 112103.

(10) Pawlikowski, J. M. Absorption Edge of Zn_3P_2. *Phys. Rev. B: Condens. Matter Mater. Phys.* **1982**, *26*, 4711−4713.

(11) Wyeth, N. C.; Catalano, A. Spectral Response Measurements of Minority-Carrier Diffusion Length in Zn_3P_2. *J. Appl. Phys.* **1979**, *50*, 1403−1407.

(12) Aleynikova, K. B.; Kozlov, A. I.; Kozlova, S. G.; Sobolev, V. V. Crystal Chemistry and Optical Properties of Monoclinic Zinc Diphosphide. *Mold. J. Phys. Sci.* **2004**, *3*, 137−148.

(13) Sobolev, V. V.; Syrbu, N. N. Optical Spectra and Energy Band Structure of the Monoclinic Crystals ZnP_2 and $ZnAs_2$. *Phys. Status Solidi* **1972**, *51*, 863−872.

(14) Gorban, I. S.; Bilyi, M. M.; Dmitruk, I. M.; Yeshchenko, O. A. Multiserial Structure of Excitonic Energy Spectrum in Monoclinic ZnP_2 Crystal. *Phys. Status Solidi* **1998**, *207*, 171−181.

(15) Shockley, W.; Queisser, H. J. Detailed Balance Limit of Efficiency of p-n Junction Solar Cells. *J. Appl. Phys.* **1961**, *32*, 510−519.

(16) Munday, J. N. The Effect of Photonic Bandgap Materials on the Shockley-Queisser Limit. *J. Appl. Phys.* **2012**, *112*, 064501.

(17) Rühle, S. Tabulated Values of the Shockley-Queisser Limit for Single Junction Solar Cells. *Sol. Energy* **2016**, *130*, 139−147.

(18) Nam, K.-H.; Hwa, Y.; Park, C.-M. Zinc Phosphides as Outstanding Sodium-Ion Battery Anodes. *ACS Appl. Mater. Interfaces* **2020**, *12*, 15053−15062.

(19) Hwang, H.; Kim, M. G.; Kim, Y.; Martin, S. W.; Cho, J. The Electrochemical Lithium Reactions of Monoclinic ZnP_2 Material. *J. Mater. Chem.* **2007**, *17*, 3161−3166.

(20) Park, C.-M.; Sohn, H.-J. Tetragonal Zinc Diphosphide and Its Nanocomposite as an Anode for Lithium Secondary Batteries. *Chem. Mater.* **2008**, *20*, 6319−6324.

(21) Živković, A.; Farkaš, B.; Uahengo, V.; de Leeuw, N. H.; Dzade, N. Y. First-Principles DFT Insights into the Structural, Elastic, and Optoelectronic Properties of α and β -ZnP_2: Implications for Photovoltaic Applications. *J. Phys.: Condens. Matter* **2019**, *31*, 265501.

(22) Futsushara, M.; Yoshioka, K.; Takai, O. Degradation of Zn_3N_2 Films Prepared by Reactive Rf Magnetron Sputtering. *J. Korean Inst. Surf. Eng.* **1996**, *29*, 563−569.

(23) Bär, M.; Ahn, K.-S.; Shet, S.; Yan, Y.; Weinhardt, L.; Fuchs, O.; Blum, M.; Pookpanratana, S.; George, K.; Yang, W.; Denlinger, J. D.; Al-Jassim, M.; Heske, C. Impact of Air Exposure on the Chemical and Electronic Structure of $ZnO:Zn_3N_2$ Thin Films. *Appl. Phys. Lett.* **2009**, *94*, 012110.

(24) Pern, F. J.; Glick, S. H.; Li, X.; DeHart, C.; Gennett, T.; Contreras, M.; Gessert, T. Stability of TCO Window Layers for Thin-Film CIGS Solar Cells upon Damp Heat Exposures: Part III. *SPIE Proceedings, Reliability of Photovoltaic Cells, Modules, Components, and Systems II*, 2009; Vol. 7412, 74120K.

(25) Dhakal, T. P.; Hamasha, M. M.; Nandur, A. S.; Vanhart, D.; Vasekar, P.; Lu, S.; Sharma, A.; Westgate, C. R. Moisture-Induced Surface Corrosion in AZO Thin Films Formed by Atomic Layer Deposition. *IEEE Trans. Device Mater. Reliab.* **2012**, *12*, 347−356.

(26) Polydorou, E.; Sakellis, I.; Soultati, A.; Kaltzoglou, A.; Papadopoulos, T. A.; Briscoe, J.; Tsikritzis, D.; Fakis, M.; Palilis, L. C.; Kennou, S.; Argitis, P.; Falaras, P.; Davazoglou, D.; Vasilopoulou, M. Avoiding Ambient Air and Light Induced Degradation in High-Efficiency Polymer Solar Cells by the Use of Hydrogen-Doped Zinc Oxide as Electron Extraction Material. *Nano Energy* **2017**, *34*, 500−514.

(27) Jeong, W.-J.; Park, G.-C. Electrical and Optical Properties of ZnO Thin Film as a Function of Deposition Parameters. *Sol. Energy Mater. Sol. Cells* **2001**, *65*, 37−45.

(28) Keis, K.; Magnusson, E.; Lindström, H.; Lindquist, S. E.; Hagfeldt, A. A 5% Efficient Photoelectrochemical Solar Cell Based on Nanostructured ZnO Electrodes. *Sol. Energy Mater. Sol. Cells* **2002**, *73*, 51−58.

(29) Gonzalez-Valls, I.; Lira-Cantu, M. Vertically-Aligned Nanostructures of ZnO for Excitonic Solar Cells: A Review. *Energy Environ. Sci.* **2009**, *2*, 19−34.

(30) Shao, L.-X.; Chang, K.-H.; Hwang, H.-L. Zinc Sulfide Thin Films Deposited by RF Reactive Sputtering for Photovoltaic Applications. *Appl. Surf. Sci.* **2003**, *212-213*, 305−310.

(31) Goudarzi, A.; Aval, G. M.; Sahraei, R.; Ahmadpoor, H. Ammonia-Free Chemical Bath Deposition of Nanocrystalline ZnS Thin Film Buffer Layer for Solar Cells. *Thin Solid Films* **2008**, *516*, 4953−4957.

(32) Ummartyotin, S.; Infahsaeng, Y. A Comprehensive Review on ZnS: From Synthesis to an Approach on Solar Cell. *Renewable Sustainable Energy Rev.* **2016**, *55*, 17−24.

(33) Bhushan, M. Schottky Solar Cells on Thin Polycrystalline Zn_3P_2 Films. *Appl. Phys. Lett.* **1982**, *40*, 51−53.

(34) Futsuhara, M.; Yoshioka, K.; Takai, O. Structural, Electrical and Optical Properties of Zinc Nitride Thin Films Prepared by Reactive Rf Magnetron Sputtering. *Thin Solid Films* **1998**, *322*, 274−281.

(35) Trapalis, A.; Heffernan, J.; Farrer, I.; Sharman, J.; Kean, A. Structural, Electrical, and Optical Characterization of as Grown and Oxidized Zinc Nitride Thin Films. *J. Appl. Phys.* **2016**, *120*, 205102.

(36) Kathalingam, A.; Mahalingam, T.; Sanjeeviraja, C. Optical and Structural Study of Electrodeposited Zinc Selenide Thin Films. *Mater. Chem. Phys.* **2007**, *106*, 215−221.

(37) Popa, M. E.; Rusu, G. I. Structural Characteristics and Optical Properties of Zinc Selenide Thin Films. *Optoelectron. Adv. Mater., Rapid Commun.* **2011**, *5*, 842−845.

(38) Chiang, C.-T.; Roberts, J. T. Surface Functionalization of Zinc Oxide Nanoparticles: An Investigation in the Aerosol State. *Chem. Mater.* **2011**, *23*, 5237−5242.

(39) Gonfa, B. A.; Da Cunha, A. F.; Timmons, A. B. ZnO Nanostructures for Photovoltaic Cells. *Phys. Status Solidi B* **2010**, *247*, 1633−1636.

(40) Brockway, L.; Van Laer, M.; Kang, Y.; Vaddiraju, S. Large-Scale Synthesis and in Situ Functionalization of Zn_3P_2 and Zn_4Sb_3 Nanowire Powders. *Phys. Chem. Chem. Phys.* **2013**, *15*, 6260−6267.

(41) Beek, W. J. E.; Wienk, M. M.; Janssen, R. A. J. Efficient Hybrid Solar Cells from Zinc Oxide Nanoparticles and a Conjugated Polymer. *Adv. Mater.* **2004**, *16*, 1009−1013.

(42) Dagar, J.; Scavia, G.; Scarselli, M.; Destri, S.; De Crescenzi, M.; Brown, T. M. Coating ZnO Nanoparticle Films with DNA Nanolayers for Enhancing the Electron Extracting Properties and Performance of Polymer Solar Cells. *Nanoscale* **2017**, *9*, 19031−19038.

(43) Tiwari, A.; Dhoble, S. J. Stabilization of ZnS Nanoparticles by Polymeric Matrices: Syntheses, Optical Properties and Recent Applications. *RSC Adv.* **2016**, *6*, 64400−64420.

(44) Ramos-Sanchez, G.; Albornoz, M.; Yu, Y.-H.; Cheng, Z.; Vasiraju, V.; Vaddiraju, S.; El Mellouhi, F.; Balbuena, P. B. Organic Molecule-Functionalized Zn_3P_2 Nanowires for Photochemical H_2 Production: DFT and Experimental Analyses. *Int. J. Hydrogen Energy* **2014**, *39*, 19887−19898.

(45) Dzade, N. Y. First-Principles Insights into the Interface Chemistry between 4-Aminothiophenol and Zinc Phosphide (Zn_3P_2) Nanoparticles. *ACS Omega* **2020**, *5*, 1025−1032.

(46) Dzade, N. Y.; Roldan, A.; de Leeuw, N. H. Surface and Shape Modification of Mackinawite (FeS) Nanocrystals by Cysteine Adsorption: A First-Principles DFT-D2 Study. *Phys. Chem. Chem. Phys.* **2016**, *18*, 32007−32020.

(47) Farkaš, B.; Terranova, U.; de Leeuw, N. H. Binding Modes of Carboxylic Acids on Cobalt Nanoparticles. *Phys. Chem. Chem. Phys.* **2020**, *22*, 985−996.

(48) Kohn, W.; Sham, L. J. Self-Consistent Equations Including Exchange and Correlation Effects. *Phys. Rev.* **1965**, *140*, A1133.

(49) Hohenberg, P.; Kohn, W. Inhomogeneous Electron Gas. *Phys. Rev.* **1964**, *136*, B864−B871.

(50) Kresse, G.; Furthmüller, J. Efficient iterative schemes forab initiototal-energy calculations using a plane-wave basis set. *Phys. Rev. B: Condens. Matter Mater. Phys.* **1996**, *54*, 11169−11186.

(51) Perdew, J. P.; Burke, K.; Ernzerhof, M. Generalized Gradient Approximation Made Simple. *Phys. Rev. Lett.* **1996**, *77*, 3865−3868.

(52) Blöchl, P. E. Projector Augmented-Wave Method. *Phys. Rev. B: Condens. Matter Mater. Phys.* **1994**, *50*, 17953−17979.

(53) Kresse, G.; Joubert, D. From Ultrasoft Pseudopotentials to the Projector Augmented-Wave Method. *Phys. Rev. B: Condens. Matter Mater. Phys.* **1999**, *59*, 1758−1775.

(54) Grimme, S.; Antony, J.; Ehrlich, S.; Krieg, H. A Consistent and Accurate Ab Initio Parametrization of Density Functional Dispersion Correction (DFT-D) for the 94 Elements H-Pu. *J. Chem. Phys.* **2010**, *132*, 154104.

(55) Watson, G. W.; Kelsey, E. T.; de Leeuw, N. H.; Harris, D. J.; Parker, S. C. Atomistic Simulation of Dislocations, Surfaces and Interfaces in MgO. *J. Chem. Soc., Faraday Trans.* **1996**, *92*, 433−438.

(56) Wulff, G. XXV. Zur Frage der Geschwindigkeit des Wachsthums und der Auflösung der Krystallflächen. *Z. für Kristallogr.—Cryst. Mater.* **1901**, *34*, 449−530.

(57) Zucker, R. V.; Chatain, D.; Dahmen, U.; Hagège, S.; Carter, W. C. New Software Tools for the Calculation and Display of Isolated and Attached Interfacial-Energy Minimizing Particle Shapes. *J. Mater. Sci.* **2012**, *47*, 8290−8302.

(58) Zanin, I. E.; Aleinikova, K. B.; Antipin, M. Y. Analysis of chemical bonding in the α and β modifications of zinc diphosphide from X-ray diffraction data. *Crystallogr. Rep.* **2003**, *48*, 199−204.

(59) Soshnikov, L. E.; Trukhan, V. M.; Golyakevich, T. V.; Soshnikova, H. L. Elastic and Dielectric Properties of $A^{II}B_2^V$ (A = Cd or Zn, B = P or As) Single Crystals. *Crystallogr. Rep.* **2005**, *50*, S37−S45.

(60) Samuel, V.; Rao, V. J. Optical and Valence Band Studies of ZnP_2 Thin Films. *J. Mater. Res.* **1989**, *4*, 185−188.

(61) Farkaš, B.; Zivkovic, A.; Uahengo, V.; Dzade, N. Y.; De Leeuw, N. H. Insights from Density Functional Theory Calculations into the Effects of the Adsorption and Dissociation of Water on the Surface Properties of Zinc Diphosphide (ZnP_2) Nanocrystals. *Phys. Chem. Chem. Phys.* **2021**, *23*, 26482−26493.

📖 Recommended by ACS